

Group Convolutional Neural Network Ground State of the Quantum Dimer Model

Ojasvi Sharma, Sandipan Manna, Prashant Shekhar Rao, and G J Sreejith
Indian Institute of Science Education and Research, Pune, India - 411008

We estimate the ground state of the square lattice Quantum Dimer Model in a p4m-symmetric Group Convolutional Neural Network (GCNN) representation and show that results in agreement with exact diagonalization (ED) and quantum Monte Carlo (QMC) can be obtained with a $\mathcal{L} = 2$ layer network. In systems of linear size $L = 8$ with Hilbert space dimension 3.1×10^8 , GCNN shows fidelity as high as 0.99999 with ED. For $12 \leq L \leq 32$, we find excellent agreement with QMC estimates of energy, order parameters and correlation functions. The network is optimized by minimizing the energy estimated from a Metropolis algorithm assisted by a directed loop sampler. We evaluate the quantum geometric tensor at the minima for $\mathcal{L} = 1, 2$ and 3 and show that the empirical quantum dimension saturates with increasing network complexity due to Metropolis sampling constraints.

Efficient quantum state representation is an important frontier of research in quantum many-body physics. General classes of representations such as tensor networks (TN) [1], quantum Monte Carlo (QMC) samples [2], and shadow representations [3] have distinct regimes of utility and limitations [4–7]; interestingly their representability can shed light on the physical structure of the state [8, 9].

Neural quantum states (NQS) employing artificial neural networks as variational ansatz have recently been proposed as a scalable representation of many-body states [10, 11]. The universal function approximation property of neural networks [12] allows NQS to represent arbitrary quantum states with sufficient parameterization. Efficiency and expressive power of different NQS architectures are being investigated in several quantum many-body contexts, with Restricted Boltzmann Machines (RBMs) being the focus of early studies due to their simplicity and correspondence with spin glass models [10, 11, 13, 14]. Even simple RBMs can express highly entangled quantum states [15], offering an alternative to TNs. Recent works in specific contexts suggest that TN states are a subset of NQS [11, 16–19] with NQS capable of capturing certain non-area-law states, thereby going beyond the manifold of TN states. RBM representations have been utilized to explore ground states of several lattice models, ranging from Ising and Heisenberg systems [10, 20] to fracton models [21] and systems possessing non-Abelian and anyonic features [22]. Deep networks and transformer architectures have been explored in describing quantum Hall states [23–25] and quantum spin liquids [26, 27]. Motivated by the success in image processing and similarity to coarse-graining [28], Convolutional Neural Networks (CNNs) have been used to represent ground states for the 2D J_1 - J_2 Heisenberg model [29, 30] up to system size 10×10 . CNNs inherently impose lattice translational symmetries. A generalization incorporating full space group symmetries – Group Convolutional Neural Networks (GCNNs) [31] were used to study ground and low-lying excited states of J_1 - J_2 model and spin- $\frac{1}{2}$ anti-ferromagnets [32–34].

We employ GCNNs to study the ground state of the

Quantum Dimer Model (QDM) on lattices of linear size up to $L=32$. GCNN for the dimer model uses a generalization of the GCNN studied previously in spin models to allow for the local degrees of freedom to transform non-trivially under the lattice symmetries. The Monte Carlo estimation of the energy and observables in the constrained model is facilitated by incorporating a directed loop algorithm in place of local spin updates. For small systems ($L \leq 8$), results obtained from $\mathcal{L}=2$ layer GCNN show excellent agreement with Exact Diagonalization (ED), while extensive benchmarking against QMC [35] show equally good agreement for larger systems with dimensions $\sim 10^{128}$ ($\dim \approx e^{0.3L^2}$ [36]). For specific choices of channels in each layer that we study, we find that $\mathcal{L}=2$ networks suffice for accurate energies, order parameters, and correlations. We find that the sampler accuracy constrains the empirical quantum geometric tensor (QGT) rank, preventing complex GCNNs with more layers from yielding better performance.

Quantum Dimer Model: A paradigmatic model of locally constrained systems is the QDM. Originally introduced [37] in the context of high- T_c superconductivity as an effective description of resonating valence bond states, QDM is one of the simplest systems exhibiting topological order and fractionalization [38]. Variants of dimer models have been of interest in combinatorics [39–42], gauge theory [43–46] and statistical mechanics [36, 47–50]. The 2D-QDM Hilbert space is made of classical fully packed hard-core dimer configurations as the basis states, with a Hamiltonian (on a square lattice) that reads as:

$$H_{\text{QDM}} = -t \sum_{\text{plaq.}} |\uparrow\downarrow\rangle\langle\downarrow\uparrow| + |\downarrow\uparrow\rangle\langle\uparrow\downarrow| + V \sum_{\text{plaq.}} |\uparrow\uparrow\rangle\langle\downarrow\downarrow| + |\downarrow\downarrow\rangle\langle\uparrow\uparrow| \quad (1)$$

Here, the first term is kinetic energy that resonantly rotates the flippable plaquettes (plaquettes with two parallel dimers) by $\pi/2$, and the second is a potential energy term that assigns an energy cost V to each flippable plaquette. We set $t = 1$ for our calculations.

The QDM phase diagram depends on the lattice geometry and dimensionality [38, 51, 52]. For $V/t > 1$ (stag-

gered phase), the ground state is highly degenerate and devoid of any flippable plaquette. As $V/t \rightarrow -\infty$, the ground state maximizes the flippable plaquettes, yielding a columnar phase with broken rotation and translational symmetry. At the RK (Rokhsar-Kivelson) point $V/t=1$, the gapless ground state is an equal-amplitude superposition of all dimer configurations. The ground state in $V/t \lesssim 1$ regime remains unresolved. Various studies have proposed a range of competing states here – columnar, plaquette, and mixed phases [35, 52–57]. This lack of consensus shows the complexity of the intermediate regime and motivates the use of complementary methods. Versatile variational techniques such as NQS provide potential new tools to address the question, and the current work demonstrates the potential of machine learning inspired methods in this and similar contexts.

Group Convolutional Neural Network: The QDM Hamiltonian is invariant under $G = \text{p4m} \cong \mathbb{Z}^2 \rtimes D_4$ symmetry of the square lattice; every element can be uniquely represented as a composition td of a translation $t \in \mathbb{Z}^2$ (modulo lattice size) and a point group element $d \in D_4$ generated by the reflection and $\frac{\pi}{2}$ rotations. Each dimer configuration can be uniquely written as a map $\sigma : \mathbb{L} \rightarrow O$, from the lattice \mathbb{L} to the set of possible dimer state $O = \{\pm\hat{x}, \pm\hat{y}\}$ on each site $\vec{r} \in \mathbb{L}$. The symmetry element $g = td$ acts on a configuration σ as $(g\sigma)_{\vec{r}} = d^{-1}(\sigma_{(g^{-1}\vec{r})})$ where g -action on \vec{r} and d -action on the local state are the natural actions of p4m and D_4 on \mathbb{L} and O respectively. Ground state of the QDM transforms under the trivial representation of the p4m. Imposing this constraint explicitly through the GCNNs improves the ansatz accuracy [31–33, 58]. Note that unlike the GCNNs studied before where configurations transformed as a scalar, the local states here transform non-trivially under G .

First layer of the GCNN maps the input configuration σ to a feature map f^1 over G :

$$f_g^{1,\alpha} = \Gamma \left[\sum_{\vec{r} \in \mathbb{L}} (g^{-1}\sigma)_{\vec{r}} K_{\vec{r}}^\alpha + b^{1,\alpha} \right], \quad g \in G \quad (2)$$

where $K : \mathbb{L} \rightarrow \mathbb{C}$ is the embedding kernel, $f^1 : G \rightarrow \mathbb{C}$ is the feature map obtained from the first layer, b^1 is the bias, and Γ is a non-linear activation function chosen as the complex version of the Scaled Exponential Linear Unit (SELU) [59] – for $x \in \mathbb{C}$, $\Gamma(x) = \text{SELU}(\Re(x)) + i\text{SELU}(\Im(x))$. The superscript $\alpha = 1, \dots, c_1$ is the channel index. For brevity, hereafter we suppress the channel indices. The embedding layer satisfies the following equivariance for any $u, g \in G$ and any configuration σ :

$$f_g(u\sigma) = f_{u^{-1}g}(\sigma). \quad (3)$$

The output of the embedding layer is further passed to $\mathcal{L}-1$ group-convolutional (GC) layers (\mathcal{L} is the number of

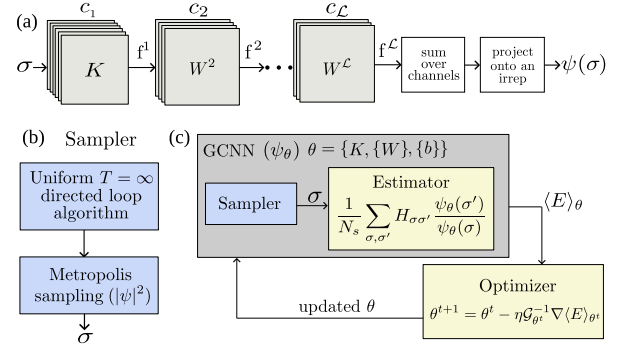


FIG. 1. (a) GCNN architecture with \mathcal{L} layers. (b) Working of the sampler. (c) Schematic of the algorithm.

layers) which take one feature map over G into another:

$$f_g^{i+1} = \text{GC}[f^i]_g := \Gamma \left[\sum_{h \in G} W_{h^{-1}g}^{i+1} f_h^i + b^{i+1} \right]. \quad (4)$$

Here W, b are the GC kernels and biases. The GCs (4) satisfy the following equivariance $\forall u \in G$:

$$\text{GC}[f^i \circ u]_g = \Gamma \left[\sum_{h \in G} W_{h^{-1}g}^{i+1} f_{uh}^i + b^{i+1} \right] = f_{ug}^{i+1} \quad (5)$$

The \mathcal{L}^{th} layer features are added and projected on an irreducible representation (irrep) of G as:

$$\psi(\sigma) = \exp \left[\sum_{g \in G} \chi_g^* \sum_{\alpha=1}^{c_{\mathcal{L}}} f_g^{\mathcal{L},\alpha} \right] \quad (6)$$

where χ_g are the characters of the irrep, and $c_{\mathcal{L}}$ is the number of channels in the \mathcal{L}^{th} layer. We project onto the trivial irrep ($\chi_g=1$). Equivariances (Eq. 3, 5) and Eq. 6 imply the invariance $\psi(u\sigma) = \psi(\sigma)$. An \mathcal{L} -layer GCNN has $c_1 L^2 + \sum_{i=1}^{\mathcal{L}-1} c_i c_{i+1} |G|^2 + \sum_{i=1}^{\mathcal{L}} c_i$ complex parameters where $|G|$ is the order of the group ($8L^2$ for p4m), and c_i is the number of channels in the i^{th} layer. We use $\mathcal{L} = 1, 2$ and 3 layers with $(2\mathcal{L}, 2(\mathcal{L}-1), \dots, 2)$ channels in the layers, following the choice in Ref. 29. Thus, networks with $\mathcal{L} = 1, 2$ and 3 have (2), (4, 2) and (6, 4, 2) channels in each layer, respectively. At $L = 8$, there are 130, 4358, 16780 complex parameters respectively.

Figure 1(a) shows the \mathcal{L} -layer GCNN which produces the p4m-invariant function $\psi_\theta(\sigma)$ parametrized by the weights and biases θ and Fig. 1(c) shows the optimization scheme (also see [60, 61]). Given an initial configuration σ , a $T=\infty$ directed loop sampler (Fig. 1(b)) proposes a new configuration σ' which is accepted with Metropolis probability $\min[1, |\psi_\theta(\sigma')|^2 / |\psi_\theta(\sigma)|^2]$. Iterating this produces $|\psi_\theta|^2$ -distributed samples. The energy expectation $\langle E \rangle_\theta$ is computed as the average of $E_{\text{loc}}(\sigma) = \sum_{\sigma'} H_{\sigma\sigma'} \psi_\theta(\sigma') / \psi_\theta(\sigma)$ estimated from the samples, and is used to update the parameters using

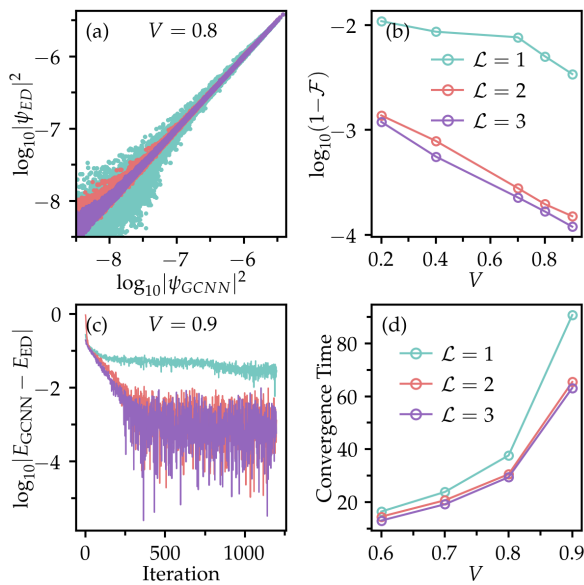


FIG. 2. (a) Comparison of $\psi(\sigma)$ from GCNN and ED at $V=0.8$. (b) Infidelity $1-\mathcal{F}$ vs V . (c) ΔE vs iterations at $V=0.9$. (d) Convergence time scale vs V . Here $L=8$, different colors show different \mathcal{L} .

stochastic reconfiguration $\theta_{\text{new}} = \theta - \eta \mathcal{G}^{-1} \nabla_{\theta} \langle E \rangle_{\theta}$ where \mathcal{G} is the quantum geometric tensor (QGT) defined as

$$[\mathcal{G}]_{ij} = \langle O_i^{\dagger} O_j \rangle - \langle O_i^{\dagger} \rangle \langle O_j \rangle, \quad O_i(\sigma) = \partial_{\theta_i} \ln \psi_{\theta}(\sigma) \quad (7)$$

where i, j index θ . We use a learning rate $\eta = 0.02$. In the following discussion, we present an extensive comparison of the GCNN with ED and QMC results. All networks are optimized by minimizing the energy estimated with 2^{12} Metropolis samples and the expectation values of observables are estimated with 2^{20} samples.

Comparison with ED: In Fig. 2, we compare the GCNN ground state with that from ED at $L = 8$ (Hilbert space dim 311, 853, 312). The GCNN performs optimization within the 628,931 dimensional p4m-invariant subspace. In Fig. 2(a) we compare $|\psi(\sigma)|^2$ obtained from GCNN and ED for $V=0.8$. Small-magnitude coefficients improve with \mathcal{L} resulting in better fidelity (See Appendix Fig. 6 for other V). The H_{QDM} commutes with the winding number (W_x, W_y) where $W_x := \sum_{\vec{r} \in \mathcal{C}_y} (-1)^{r_y} n_x(\vec{r})$ where r_y is the y -coordinate of the lattice site \vec{r} , \mathcal{C}_y are the lattice sites at a fixed r_x , and $n_x(\vec{r}) = \delta_{\sigma_{\vec{r}}, +x}$. Analogous definition applies to W_y with x and y interchanged. The ground state is in the $(W_x, W_y) = (0, 0)$ sector for $V < 1$. The GCNN ground state's components in the $W \neq 0$ sectors (dim 1.58×10^8) are negligible ($\langle \psi_{\text{GCNN}} | \Pi_{(W_x, W_y) \neq (0, 0)} | \psi_{\text{GCNN}} \rangle \approx 10^{-5}$) though the winding number constraint is not imposed on the GCNN. We find an increased fidelity, $\mathcal{F} := |\langle \psi_{\text{ED}} | \psi_{\text{GCNN}} \rangle|^2$ as V approaches the critical, RK point (Fig. 2(b)). For a given V , \mathcal{F} increases as \mathcal{L} goes from 1 to 2, but shows little gain from $\mathcal{L}=2$ to 3. The behavior can be rationalized

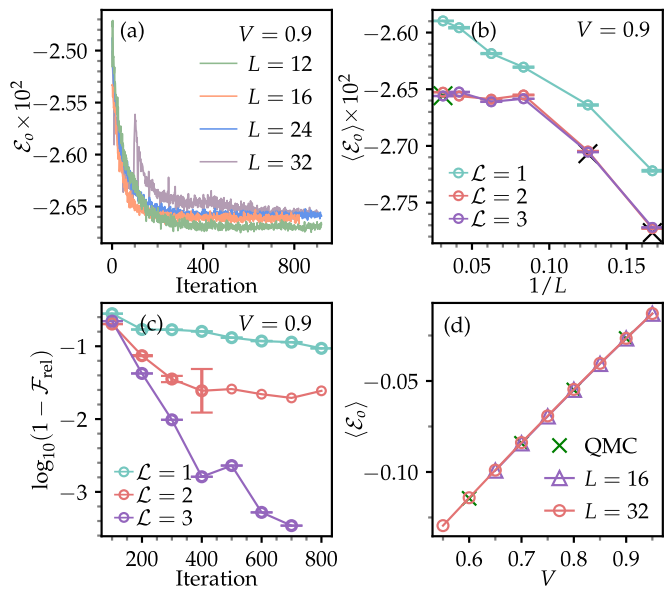


FIG. 3. (a) Energy density \mathcal{E}_o vs iteration for $(V, \mathcal{L}) = (0.9, 3)$. (b) Energy density $\langle \mathcal{E}_o \rangle$ (averaged over the last 80 iterations) as a function of L for $\mathcal{L} = 1, 2, 3$. (c) Variational fidelity between GCNNs (ref. state - $\mathcal{L}=3$, 800th iteration) as a function of iteration for $(L, V) = (12, 0.9)$. (d) $\langle \mathcal{E}_o \rangle$ for $\mathcal{L} = 3$ as a function of V . Green and black crosses indicate QMC [35] and ED results, respectively.

by the QGT rank saturation (see below). E_{GCNN} converges exponentially towards E_{ED} with iterations until saturation due to sampling errors (Fig. 2(c)). Convergence time-scale in iterations (Fig. 2(d)) increase with V as RK point is approached but at the RK point, where $\psi(\sigma)$ is a constant, GCNN optimizes in 10 iterations.

Comparison with QMC: Having benchmarked GCNN against the largest system accessible by ED, we extend our study to $12 \leq L \leq 32$ in Fig. 3. Figure 3(a) presents the convergence of energy density \mathcal{E}_o (per plaquette) with iterations showing that convergence time weakly increase with L . Figure 3(b) shows energy density $\langle \mathcal{E}_o \rangle$ as a function of $1/L$ obtained from GCNNs with $\mathcal{L}=1, 2, 3$ layers. Here we also compare our GCNN results with QMC results from [35], where we observe the best match for $\mathcal{L}=2, 3$ results. In Fig. 3(c), we study the iteration dependence of fidelity (\mathcal{F}_{rel}) between GCNNs by estimating the fidelity (See Appendix) of the state at intermediate iterations with $\mathcal{L}=3$ layered GCNN obtained in the 800th iteration. Fidelity increases slowly but steadily in the $\mathcal{L} = 1$ case but saturates in the $\mathcal{L} = 2$ case. Note that the steady increase in fidelity in $\mathcal{L} = 3$ is an artefact of biased choice of the reference state. Figure 3(d) energy density \mathcal{E}_o as a function of V obtained by $\mathcal{L} = 3$ GCNN. The results are in excellent agreement with QMC calculations[35].

Columnar order: Agreement in the variational energies with QMC is a poor evidence for the fidelity of the GCNN ansatz. Since explicit fidelity estimation

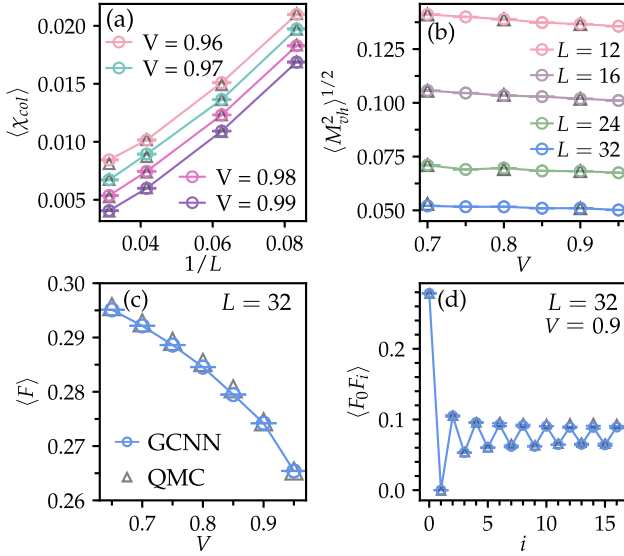


FIG. 4. (a) $\langle \chi_{\text{col}} \rangle$ as a function of L for different V . (b) Expectation value of nematic order parameter as a function of V for $L=12, 16, 24$ and 32 . The errorbars are smaller than the marker size. (c) Expectation value of flip operator per plaquette as function of V for $L=32$. (d) Two-point correlation of flip operator as a function of diagonal separation $\vec{r}_i = (i, i)$ at $(L, V) = (32, 0.9)$. Panels (a) to (d) compare GCNN results (circles) with QMC results (triangles) in [35].

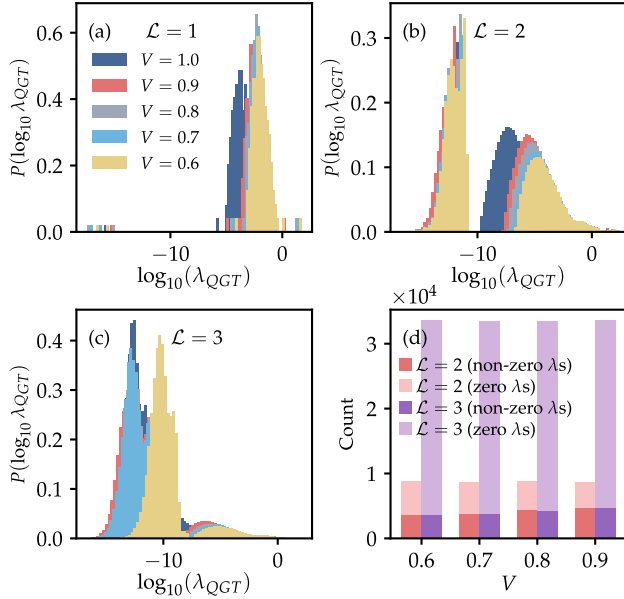


FIG. 5. Probability distribution of the QGT eigenvalues for the $L = 8$ GCNN with (a) $\mathcal{L} = 1$ layers (b) $\mathcal{L} = 2$ layers (c) $\mathcal{L} = 3$ layers (d) Count of zero and non-zero eigenvalues of QGT for $\mathcal{L} = 2$ and 3 . The number of non-zero eigenvalues do not change going from $\mathcal{L} = 2$ to $\mathcal{L} = 3$ GCNN, indicating the redundant directions in the energy landscape where the change in parameters do not lead to change in the cost function.

is not feasible in larger systems, we now compare order parameter expectation values and correlations calculated in the GCNN states with QMC. We first consider the columnar order parameter \vec{N} with $N_{x(y)} = \frac{1}{2L^2} \sum_{\vec{r}} (-1)^{r_x(r_y)} n_{x(y)}(\vec{r})$. We present $\langle \chi_{\text{col}} \rangle = \langle |\vec{N}|^2 \rangle$ at V close to the RK point for different L in Fig. 4(a). χ_{col} decreases as L increases and $V/t \rightarrow 1$ closely matching the QMC results. The full distribution of the columnar order parameter in the quantum ground state for different values of V and $L = 32$ are shown in Appendix Fig. 8 showing the emergence of full rotation symmetry in larger systems.

Nematic order: Next we consider the nematic order parameter defined by $M_{vh} = \frac{2}{L^2} (N_v - N_h)$ where N_v and N_h are the number of vertical and horizontal dimers respectively. We study $\langle M_{vh}^2 \rangle^{1/2}$ for various V close to RK point across system sizes in Fig. 4(b) again demonstrating excellent agreement with QMC.

Plaquette flip operator: All observables compared so far, other than energy, are diagonal in the dimer basis. Next, we calculate the Flip operator per plaquette, $F := \frac{1}{L^2} \sum_{\text{plaq.}} |\uparrow\downarrow\rangle\langle\uparrow\downarrow| + |\downarrow\uparrow\rangle\langle\downarrow\uparrow|$, which counts the number of resonating plaquettes. It can be defined in term of energy expectation value as, $\langle F \rangle = -\mathcal{E}_o + V \frac{\langle N_f \rangle}{L^2}$. where $\langle N_f \rangle$ is the number of flippable plaquettes. In Fig. 4(c), we obtain $\langle F \rangle$ for linear system size $L=32$.

Correlation functions: We now look at the two point correlation function of F . Note that unlike the $\langle F \rangle$, $\langle F_0 F_i \rangle$ cannot be estimated using a diagonal observable and is obtained by defining an estimator analogous to E_{loc} . The result is presented in Fig. 4(d) for $L = 32$ and $V = 0.9$ which shows oscillation with slowly decaying envelope.

Having demonstrated the validity of the GCNN ansatz by benchmarking with ED and QMC, we briefly look at the nature of energy landscape in the vicinity of the optimal parameters. The non-zero eigenvalues of the QGT represent directions which have been optimized in reaching the saturation of the energy time series and null vectors represent flat directions unusable (in a given iteration) to improve the variational energy [62]. While the true rank of the QGT can be large, in the energy landscape approximated using a mini-batch of Monte Carlo samples, the empirical rank of QGT is lower resulting in not all available parameters efficiently reaching the optimum. Figure 5 shows the probability distribution of log of the QGT eigenvalues calculated in a 2^{12} -sample energy landscape estimate. All eigenvalues are non-zero in the one layer network, whereas there is a large number of zero eigenvalues in the $\mathcal{L} = 2, 3$ layer networks. The number of non-zero eigenvalues do not change with increasing network complexity consistent with absence of improvement in the fidelities. The observation is true for all V studied. Consistent with this picture, the QGT rank estimated on the 2^{13} and 2^{14} -sample energy landscape has higher rank

as shown in the Appendix Fig. 9 potentially suggesting strategies to better fidelities in simpler networks.

We thank O Syljuasen for sharing numerical results from calculations in previous publications. GJS thanks D Kalra, S Powell, F Alet and K Damle for valuable discussions in previous projects. We acknowledge the use of NetKet [60, 61] in performing the numerical calculations presented in this work. We thank National Supercomputing Mission for providing computing resources of “PARAM Brahma” at IISER Pune, implemented by C-DAC and supported by the Ministry of Electronics and Information Technology (MeitY) and Department of Science and Technology (DST), Government of India. GJS thanks IHUB Quantum Technology foundation for financial support. OS acknowledges financial support from the Council of Scientific and Industrial Research (CSIR), India in the form of Junior Research Fellowship 22D/23J02781.

-
- [1] S. R. White, Density matrix formulation for quantum renormalization groups, *Physical Review Letters* **69**, 2863 (1992).
- [2] A. W. Sandvik, Computational Studies of Quantum Spin Systems, *AIP Conference Proceedings* **1297**, 135 (2010), publisher: AIP Publishing.
- [3] S. Aaronson, Shadow Tomography of Quantum States, *SIAM Journal on Computing* **49**, STOC18 (2020), num Pages: STOC18-394 Publisher: Society for Industrial and Applied Mathematics.
- [4] E. Y. Loh, J. E. Gubernatis, R. T. Scalettar, S. R. White, D. J. Scalapino, and R. L. Sugar, Sign problem in the numerical simulation of many-electron systems, *Physical Review B* **41**, 9301 (1990), publisher: American Physical Society.
- [5] P. Henelius and A. W. Sandvik, Sign problem in Monte Carlo simulations of frustrated quantum spin systems, *Physical Review B* **62**, 1102 (2000), publisher: American Physical Society.
- [6] N. Schuch, M. M. Wolf, F. Verstraete, and J. I. Cirac, Computational Complexity of Projected Entangled Pair States, *Physical Review Letters* **98**, 140506 (2007), publisher: American Physical Society.
- [7] L. Tagliacozzo, G. Evenbly, and G. Vidal, Simulation of two-dimensional quantum systems using a tree tensor network that exploits the entropic area law, *Physical Review B* **80**, 235127 (2009).
- [8] M. B. Hastings, Obstructions to classically simulating the quantum adiabatic algorithm, *Quantum Info. Comput.* **13**, 1038 (2013).
- [9] B. Swingle, Entanglement renormalization and holography, *Physical Review D* **86**, 065007 (2012).
- [10] G. Carleo and M. Troyer, Solving the quantum many-body problem with artificial neural networks, *Science* **355**, 602 (2017), publisher: American Association for the Advancement of Science.
- [11] X. Gao and L.-M. Duan, Efficient representation of quantum many-body states with deep neural networks, *Nature Communications* **8**, 662 (2017), publisher: Nature Publishing Group.
- [12] K. Hornik, M. Stinchcombe, and H. White, Multilayer feedforward networks are universal approximators, *Neural Networks* **2**, 359 (1989).
- [13] Y. Nomura, A. S. Darmawan, Y. Yamaji, and M. Imada, Restricted Boltzmann machine learning for solving strongly correlated quantum systems, *Physical Review B* **96**, 205152 (2017).
- [14] Y. Nomura, Helping restricted Boltzmann machines with quantum-state representation by restoring symmetry, *Journal of Physics: Condensed Matter* **33**, 174003 (2021), publisher: IOP Publishing.
- [15] D.-L. Deng, X. Li, and S. Das Sarma, Quantum Entanglement in Neural Network States, *Physical Review X* **7**, 021021 (2017).
- [16] Y. Zheng, H. He, N. Regnault, and B. A. Bernevig, Restricted Boltzmann machines and matrix product states of one-dimensional translationally invariant stabilizer codes, *Physical Review B* **99**, 155129 (2019).
- [17] O. Sharir, A. Shashua, and G. Carleo, Neural tensor contractions and the expressive power of deep neural quantum states, *Physical Review B* **106**, 205136 (2022).
- [18] Y. Huang and J. E. Moore, Neural Network Representation of Tensor Network and Chiral States, *Physical Review Letters* **127**, 170601 (2021).
- [19] D. Wu, R. Rossi, F. Vicentini, and G. Carleo, From tensor-network quantum states to tensorial recurrent neural networks, *Physical Review Research* **5**, L032001 (2023).
- [20] L. L. Viteritti, F. Ferrari, and F. Becca, Accuracy of restricted Boltzmann machines for the one-dimensional J_1 - J_2 Heisenberg model, *SciPost Physics* **12**, 166 (2022).
- [21] M. Machaczek, L. Pollet, and K. Liu, Neural quantum state study of fracton models, *SciPost Physics* **18**, 112 (2025).
- [22] T. Vieijra, C. Casert, J. Nys, W. De Neve, J. Haegeman, J. Ryckebusch, and F. Verstraete, Restricted Boltzmann Machines for Quantum States with Non-Abelian or Anyonic Symmetries, *Physical Review Letters* **124**, 097201 (2020).
- [23] Y. Teng, D. D. Dai, and L. Fu, Solving and visualizing fractional quantum Hall wavefunctions with neural network (2024), arXiv:2412.00618 [cond-mat].
- [24] D. Luo, T. Zaklamba, and L. Fu, Solving fractional electron states in twisted MoTe_2 with deep neural network (2025), arXiv:2503.13585 [cond-mat].
- [25] X. Li, Y. Chen, B. Li, H. Chen, F. Wu, J. Chen, and W. Ren, Deep Learning Sheds Light on Integer and Fractional Topological Insulators (2025), arXiv:2503.11756 [cond-mat].
- [26] L. L. Viteritti, R. Rende, and F. Becca, Transformer Variational Wave Functions for Frustrated Quantum Spin Systems, *Physical Review Letters* **130**, 236401 (2023).
- [27] Y. Qian, T. Zhao, J. Zhang, T. Xiang, X. Li, and J. Chen, Describing Landau Level Mixing in Fractional Quantum Hall States with Deep Learning, *Physical Review Letters* **134**, 176503 (2025).
- [28] P. Mehta and D. J. Schwab, An exact mapping between the Variational Renormalization Group and Deep Learning (2014), arXiv:1410.3831 [stat].
- [29] K. Choo, T. Neupert, and G. Carleo, Two-dimensional frustrated $J_1 - J_2$ model studied with neural network quantum states, *Physical Review B* **100**, 125124 (2019).

- [30] X. Liang, W.-Y. Liu, P.-Z. Lin, G.-C. Guo, Y.-S. Zhang, and L. He, Solving frustrated quantum many-particle models with convolutional neural networks, *Physical Review B* **98**, 104426 (2018).
- [31] T. S. Cohen and M. Welling, *Group Equivariant Convolutional Networks* (2016), arXiv:1602.07576 [cs].
- [32] C. Roth and A. H. MacDonald, *Group Convolutional Neural Networks Improve Quantum State Accuracy* (2021), arXiv:2104.05085 [quant-ph].
- [33] C. Roth, A. Szabó, and A. H. MacDonald, High-accuracy variational Monte Carlo for frustrated magnets with deep neural networks, *Physical Review B* **108**, 054410 (2023).
- [34] T. Duric, J. H. Chung, B. Yang, and P. Sengupta, Spin-1 / 2 Kagome Heisenberg Antiferromagnet: Machine Learning Discovery of the Spinon Pair-Density-Wave Ground State, *Physical Review X* **15**, 011047 (2025).
- [35] O. F. Syljuåsen, Plaquette phase of the square-lattice quantum dimer model: Quantum Monte Carlo calculations, *Physical Review B* **73**, 245105 (2006).
- [36] M. E. Fisher, Statistical Mechanics of Dimers on a Plane Lattice, *Physical Review* **124**, 1664 (1961).
- [37] D. S. Rokhsar and S. A. Kivelson, Superconductivity and the Quantum Hard-Core Dimer Gas, *Physical Review Letters* **61**, 2376 (1988).
- [38] R. Moessner and K. S. Raman, *Quantum dimer models* (2008), arXiv:0809.3051 [cond-mat].
- [39] N. Allegra, Exact solution of the 2d dimer model: Corner free energy, correlation functions and combinatorics, *Nuclear Physics B* **894**, 685 (2015).
- [40] R. Kenyon and R. Pemantle, Double-dimers, the Ising model and the hexahedron recurrence, *Journal of Combinatorial Theory, Series A* **137**, 27 (2016).
- [41] H. Jenne, Combinatorics of the double-dimer model, *Advances in Mathematics* **392**, 107952 (2021).
- [42] R. Kenyon, *Lectures on Dimers* (2009), arXiv:0910.3129 [math].
- [43] F. S. Nogueira and Z. Nussinov, Renormalization, duality, and phase transitions in two- and three-dimensional quantum dimer models, *Physical Review B* **80**, 104413 (2009).
- [44] U. Borla, B. Jeevanesan, F. Pollmann, and S. Moroz, Quantum phases of two-dimensional Z_2 gauge theory coupled to single-component fermion matter, *Physical Review B* **105**, 075132 (2022).
- [45] A. Hanany and K. D. Kennaway, *Dimer models and toric diagrams* (2005), arXiv:hep-th/0503149.
- [46] G. Misguich, D. Serban, and V. Pasquier, Quantum Dimer Model on the Kagome Lattice: Solvable Dimer-Liquid and Ising Gauge Theory, *Physical Review Letters* **89**, 137202 (2002).
- [47] M. E. Fisher and J. Stephenson, Statistical Mechanics of Dimers on a Plane Lattice. II. Dimer Correlations and Monomers, *Physical Review* **132**, 1411 (1963).
- [48] A. Giuliani and F. L. Toninelli, Non-integrable dimer models: universality and scaling relations, *Journal of Mathematical Physics* **60**, 103301 (2019), arXiv:1905.04011 [math].
- [49] C. Boutillier and B. D. Tilière, *Statistical mechanics on isoradial graphs* (2010), arXiv:1012.2955 [math].
- [50] R. Dijkgraaf, D. Orlando, and S. Reffert, *Dimer Models, Free Fermions and Super Quantum Mechanics* (2007), arXiv:0705.1645 [hep-th].
- [51] B. Dabholkar, G. J. Sreejith, and F. Alet, Reentrance effect in the high-temperature critical phase of the quantum dimer model on the square lattice, *Physical Review B* **106**, 205121 (2022).
- [52] Z. Yan, Y. Wu, C. Liu, O. F. Syljuåsen, J. Lou, and Y. Chen, Sweeping cluster algorithm for quantum spin systems with strong geometric restrictions, *Physical Review B* **99**, 165135 (2019).
- [53] O. F. Syljuåsen, Continuous-time diffusion Monte Carlo method applied to the quantum dimer model, *Physical Review B* **71**, 020401 (2005).
- [54] A. Ralko, D. Poilblanc, and R. Moessner, Generic Mixed Columnar-Plaquette Phases in Rokhsar-Kivelson Models, *Physical Review Letters* **100**, 037201 (2008).
- [55] D. Banerjee, M. Bögli, C. P. Hofmann, F.-J. Jiang, P. Widmer, and U.-J. Wiese, Interfaces, strings, and a soft mode in the square lattice quantum dimer model, *Physical Review B* **90**, 245143 (2014).
- [56] D. Banerjee, M. Bögli, C. P. Hofmann, F.-J. Jiang, P. Widmer, and U.-J. Wiese, Finite-volume energy spectrum, fractionalized strings, and low-energy effective field theory for the quantum dimer model on the square lattice, *Physical Review B* **94**, 115120 (2016).
- [57] Z. Yan, Z. Zhou, O. F. Syljuåsen, J. Zhang, T. Yuan, J. Lou, and Y. Chen, Widely existing mixed phase structure of the quantum dimer model on a square lattice, *Physical Review B* **103**, 094421 (2021).
- [58] S. d'Ascoli, L. Sagun, J. Bruna, and G. Biroli, *Finding the Needle in the Haystack with Convolutions: on the benefits of architectural bias* (2020), arXiv:1906.06766 [cs].
- [59] G. Klambauer, T. Unterthiner, A. Mayr, and S. Hochreiter, Self-Normalizing Neural Networks, in *Advances in Neural Information Processing Systems*, Vol. 30 (Curran Associates, Inc., 2017).
- [60] G. Carleo, K. Choo, D. Hofmann, J. E. Smith, T. Westerhout, F. Alet, E. J. Davis, S. Efthymiou, I. Glasser, S.-H. Lin, M. Mauri, G. Mazzola, C. B. Mendl, E. Van Nieuwenburg, O. O'Reilly, H. Théveniaut, G. Torlai, F. Vicentini, and A. Wietek, NetKet: A machine learning toolkit for many-body quantum systems, *SoftwareX* **10**, 100311 (2019).
- [61] F. Vicentini, D. Hofmann, A. Szabó, D. Wu, C. Roth, C. Giuliani, G. Pescia, J. Nys, V. Vargas-Calderón, N. Astrakhantsev, and G. Carleo, NetKet 3: Machine Learning Toolbox for Many-Body Quantum Systems, *SciPost Physics Codebases* , 7 (2022).
- [62] S. Dash, L. Gravina, F. Vicentini, M. Ferrero, and A. Georges, Efficiency of neural quantum states in light of the quantum geometric tensor, *Communications Physics* **8**, 1 (2025), publisher: Nature Publishing Group.

Additional Results

Variational energy: We extend our results (shown in Fig. 2) for different V values ($V=0.6, 0.7, 0.8, 0.9$) in Fig. 6. We observe a nice convergence to the exact ground state (shown as the bottom-most black dotted line) for all values of V . We also show a few excited states (obtained from ED) for $L=8$ in Fig. 6. Here, it is worth noting that the fluctuations in the estimated energies are much smaller than the exact energy gap. We observe that the convergence time increases as we move towards the

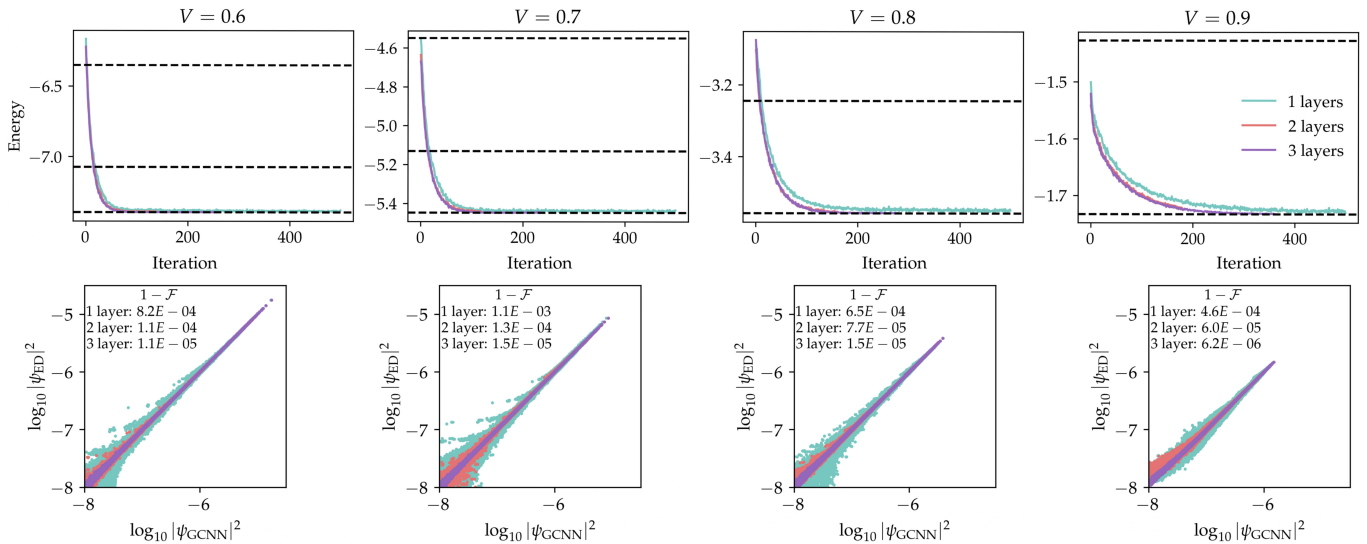


FIG. 6. First row: convergence of energy with iteration for $V = 0.6, 0.7, 0.8$ and 0.9 on an 8×8 lattice. The different black dotted lines are the energy values obtained from ED calculation for the ground state and first few excited states. Second row: Comparison between square of wavefunction amplitudes for $(0, 0)$ winding sector p4m-invariant states obtained from GCNN and ED calculations.

RK point, which is consistent with the results in Fig. 2. We also compare the coefficients $(|\psi(\sigma)|^2)$ obtained from GCNN and ED for the mentioned values of V . In Fig. 7, we present energy density \mathcal{E}_o – energy per plaquette – for various combinations of (L, V, \mathcal{L}) for $12 \leq L \leq 32$ and $\mathcal{L} = 1, 2, 3$ layers in the GCNN. We observe that $\mathcal{L}=2$ GCNN gives as good results as a $\mathcal{L}=3$ GCNN. To investigate the convergence behavior, we monitor the energy density as a function of iteration during the training of GCNNs, and find that the convergence time increases with V . Notably, once a network is trained for a given value of the interaction parameter V , we use its optimized parameters as the initial seed for training at a nearby V value. We observe that this warm-start strategy leads to significantly faster convergence compared to training from a random initialization. We benchmark our results against QMC calculations for $L = 32$ [35], and find excellent agreement between the two, confirming the reliability of our approach. The three black horizontal lines in Fig. 7 correspond to the QMC estimates of the energy density for different winding sectors. We observe that the energy fluctuations are smaller than the gap between energies of different winding sectors.

Columnar order parameter distribution: We present the N_x, N_y distribution in Fig. 8 for $L = 24$ for different values of V close to the RK point. The peak of the distributions show full rotational symmetry, with a radius that decreases as V increases, consistent with the decrease in columnar order parameter as V approaches 1.

In Fig. 9, we present QGT spectra for $(L, V, \mathcal{L}) = (8, 0.8, 2)$ estimated using 2^{10} to 1.2×10^4 Metropolis samples. Different lines indicate estimates from different Monte Carlo samples. Interestingly, the distribution

converges with sample size for $> 2^{13}$ samples and variation across trials gets suppressed with increasing sample size. More importantly, the empirical rank of the QGT appears to increase with the number of samples used to estimate the QGT. For large number of samples, the non-zero eigenvalues have a double peak distribution. It is unclear what the two scales represent.

Fidelity between two GCNNs

Here we describe the estimation of the overlap between two different NQSs ψ and ϕ . The overlap between the states is given by:

$$\langle \phi | \psi \rangle = \sum_{\{\sigma\} \in \mathcal{H}} \frac{\phi^*(\sigma) \psi(\sigma)}{\sqrt{\mathcal{N}_\phi \mathcal{N}_\psi}}$$

This sum is over all the basis states in the Hilbert space, which becomes intractable for larger system sizes where the Hilbert space dimension grows exponentially, and \mathcal{N} is not known for the same reason. We first estimate the following by sampling N_s^ϕ and N_s^ψ configurations from $|\phi(\sigma)|^2$ and $|\psi(\sigma)|^2$ respectively

$$\begin{aligned} \frac{\langle \phi | \psi \rangle}{\langle \phi | \phi \rangle} &\approx \frac{1}{N_s^\phi} \sum_{\sigma \sim |\phi(\sigma)|^2} \frac{\psi_\theta(\sigma)}{\phi_\alpha(\sigma)} \\ \frac{\langle \psi | \phi \rangle}{\langle \psi | \psi \rangle} &\approx \frac{1}{N_s^\psi} \sum_{\sigma \sim |\psi(\sigma)|^2} \frac{\phi_\theta(\sigma)}{\psi_\alpha(\sigma)} \end{aligned}$$

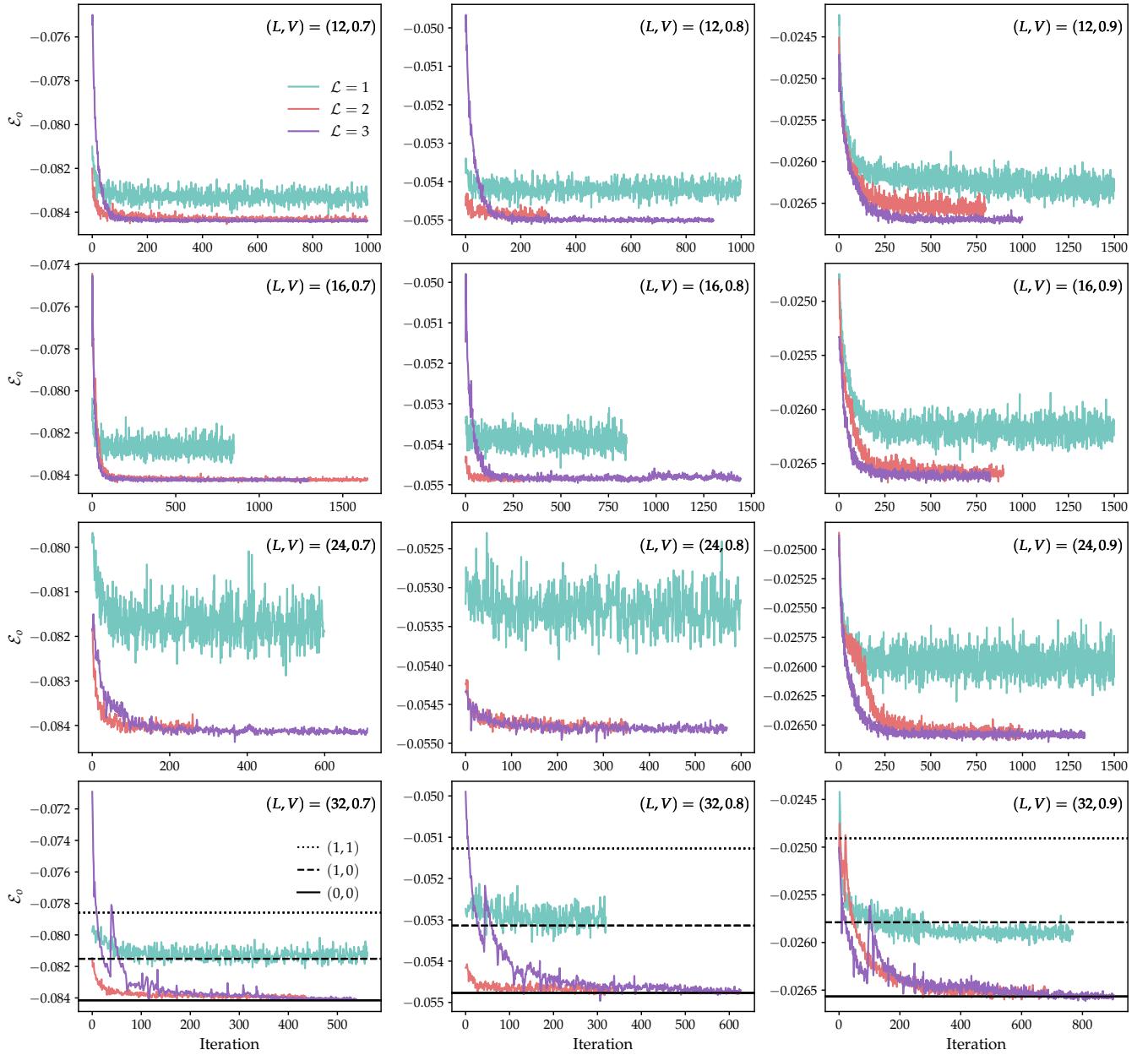


FIG. 7. Energy density as a function of iteration for $12 \leq L \leq 32$, $V = \{0.7, 0.8, 0.9\}$ and $\mathcal{L} = \{1, 2, 3\}$. For $L = 32$, the horizontal lines correspond to the QMC estimates of energy density in different winding sectors taken from [35]

The fidelity (overlap square) between the two GCNNs is estimated as

$$\mathcal{F}_{rel} = \frac{\langle \phi | \psi \rangle \langle \psi | \phi \rangle}{\langle \phi | \phi \rangle \langle \psi | \psi \rangle} \approx \frac{1}{N_{\text{samples}}^2} \sum_{i=1}^{N_s^\phi} \frac{\psi_\theta(\sigma_i)}{\phi_\alpha(\sigma_i)} \sum_{i=1}^{N_s^\psi} \frac{\phi_\alpha(\sigma_i)}{\psi_\theta(\sigma_i)} \quad (8)$$

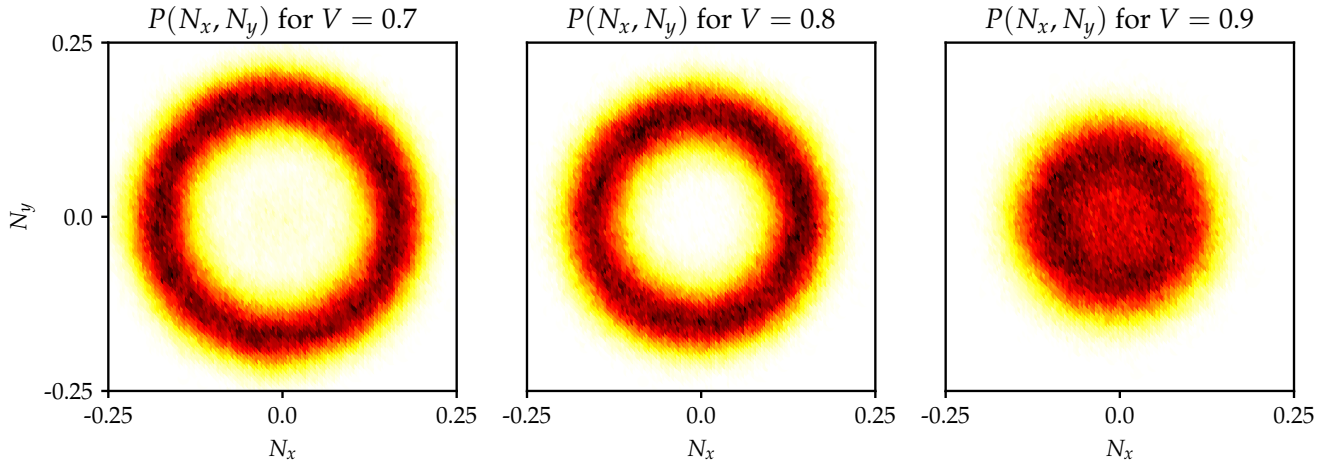


FIG. 8. Distribution of N_x, N_y (see main text) for a system with linear size $L = 24$ for different V close to the RK point.

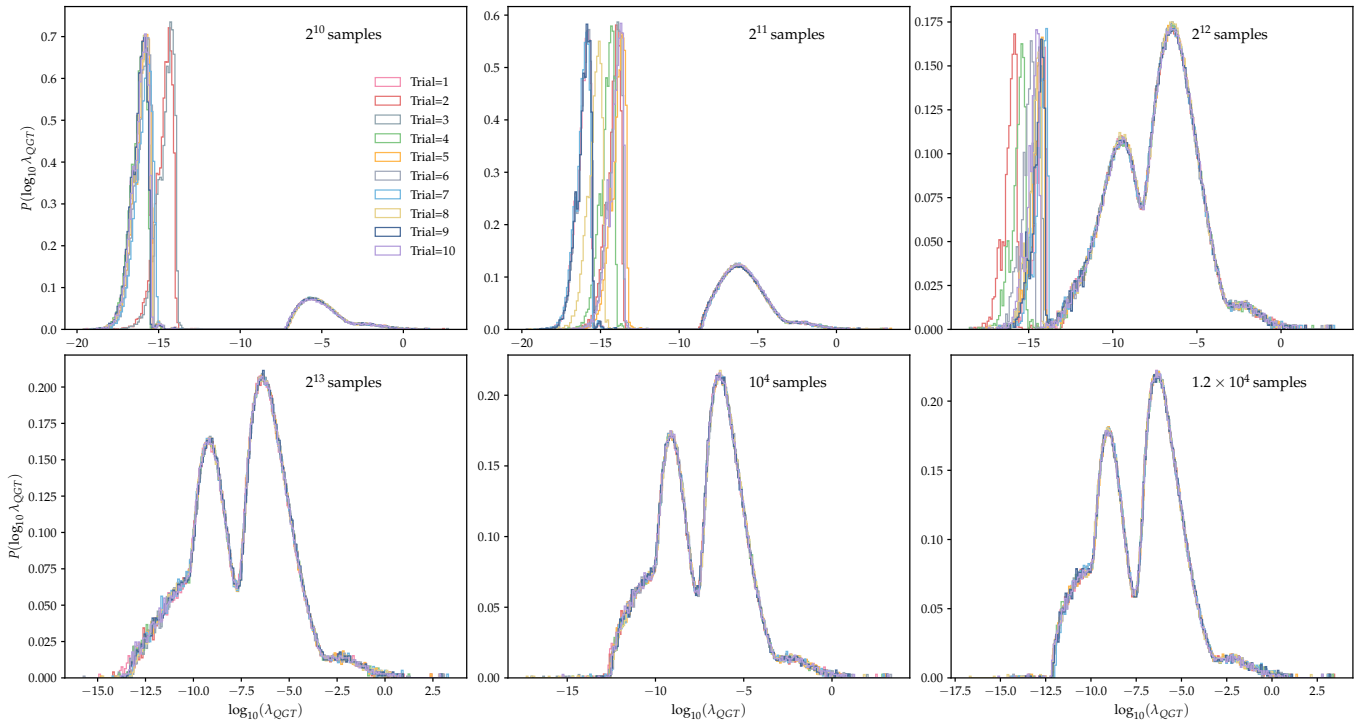


FIG. 9. Spectra of empirically estimated QGT using different choices of samples for the ground state at $V = 0.8$ of a system with linear size $L = 8$ and $\mathcal{L} = 2$. The number of zero eigenvalues decrease steadily with increasing number of samples used to estimate the landscape.